IOP Publishing Smart Materials and Structures
Smart Mater. Struct. **28** (2019) 015004 (14pp) https://doi.org/10.1088/1361-665X/aaeb6a

Wireless power transfer system with center-clamped magneto-mechano-electric (MME) receiver: model validation and efficiency investigation

Binh Duc Truong and Shad Roundy

Department of Mechanical Engineering, University of Utah, 1495 E. 100 S., 1550 MEK, Salt Lake City, UT 84112, United States of America

E-mail: Binh.D.Truong@utah.edu

Received 6 July 2018, revised 21 October 2018
Accepted for publication 25 October 2018
Published 20 November 2018

Abstract

This paper presents a complete equivalent circuit model for a wireless power transfer concept utilizing a center-clamped piezoelectric cantilever beam with magnetic tip masses as a receiver. The analytical solution for the power delivered to a load resistance is given as a function of material properties, beam characteristics and external magnetic field strength. The lumped element model is experimentally verified. The efficiency of the system is thoroughly investigated and validated. The essential effect of the coil resistance is highlighted. The analyses show that optimization of transmitter coil size and geometry of the piezoelectric transducer has a significant impact on the transduction factor between the magnetic-mechanical-electrical domains, which greatly improves the transmission efficiency. Finally, the model for evaluating the efficiency is generalized for other similar structures.

Keywords: wireless power transfer, energy conversion/generation, transmission efficiency

(Some figures may appear in colour only in the online journal)

Nomenclature

H_{ac}	AC magnetic field of the Helmholtz coils	ϵ_{33}^{S}	permittivity component at constant strain
M_B	pure moment acts on the magnet tip mass M	e_{31}	piezoelectric stress constant
J_r	remanent magnetic polarization	d_{31}	piezoelectric charge constant
V_M	volume of the magnet tip mass	b	mechanical damping coefficient
F_M	equivalent force corresponding to the moment induced by magnetic field	L_m	dimension of the cubic magnet
		M	magnet mass
l_{eff}	effective length	$2L_g$	total width of the anchor
m	effective mass of the piezoelectric transducer	K_0	short circuit stiffness
m_b	beam mass	K_1	open circuit stiffness
$(YI)_c$	flexural rigidity of the composite beam	Γ_P	electromechanical transduction factor
Y_p (t_p)	elasticity constants (thickness) of the piezoelectric layers	Γ_M	electrodynamic transduction factor
		C_0	nominal capacitance of the piezoelectric transducer
Y_s (t_s)	elasticity constants (thickness) of the shim		
w	beam width	R_L	load resistance

ζ	dimentionless damping ratio, $\zeta = b/(2m\omega_0)$
L_H	total inductance of the Helmholtz coil
R_H	parasitic resistance of the Helmholtz coil
V_s	source voltage
R_s	source resistance
Ψ	electromagnetic transduction factor
L_0	internal inductance of electromagnetic transducer

1. Introduction

Energy harvesting (EH) and wireless power transfer (WPT) provide means to power electronics while avoiding battery replacement, especially for autonomous wireless sensor nodes and wearable or implantable devices [1–6]. Toward sensing systems for human health monitoring, it should be noted that the power obtained from EH systems strongly depends on human activities, which vary remarkably during the day [7, 8]. Meanwhile, WPT provides the advantage that power from a source can be controlled and delivered to an electrical load actively and directly [9]. The latter technique, therefore, has gained more and more attention from researchers in the last decade.

Non-radiative (or near-field) WPT/charging systems are used in a wide variety of applications such as smart phones, unmanned aerial vehicles and biomedical electronics [10], utilizing capacitive or inductive coupling [11, 12]. However, the operating frequency of these technologies is typically in the range of MHz, which constrains the amplitude of the magnetic fields that can be applied to humans due to safety standards [13, 14].

One approach to overcome this challenge was to use an electromagnetic (electrodynamic) transducer as a receiver [9]. The authors later developed similar methods to extend the transmission range for bio-implants and wearables with torsional springs and a rotating magnet mass [15–17]. For harvesting energy from current-carrying conductors [18] or ambient low-frequency magnetic fields [19, 20], an alternative technique is to utilize a piezoelectric cantilever beam (either d_{31} or d_{33} coupling) with a permanent magnet placed at its tip. The mechanical resonance frequency of the electromechanical and electrodynamic receivers can be designed much lower than 1 kHz, allowing much higher external magnetic flux densities. Besides, the piezoelectric and electromagnetic generators can also scavenge energy from vibrations when the user is moving and there is no power transmitted. Several authors mentioned above have attempted to model those structures. However, these developments were either specific to particular devices and did not reflect the generalized problem, or lack of details in describing the complete model.

A more recent WPT architecture is based on the magneto-electric (ME) effect in composites of magnetostrictive and piezoelectric materials [21–24]. Most authors only investigated the power transferred to a load resistance through experiments, and did not fully address the system efficiency. In addition, observing that there is a similarity among the four resonator types (i.e. electrostatic, electromagnetic, piezoelectric and ME transducers), we are motivated to explore a complete unified-model considering both transmitting and receiving sides that can cover all four types.

In this work, we propose a symmetric structure when the bimorph piezoelectric beam is clamped at the middle and two magnet masses are attached at the two ends. We develop a theoretical lumped element model to analyze and predict system performance, which is then verified by an experimental prototype. Although the transmission efficiency is not a key metric for low power systems, it is still of interest and worthy of analysis. Both the output power and the system efficiency are derived from the equivalent circuit models.

2. Lumped-parameter model of the piezoelectric receiver

2.1. Linear two-port model

Figure 1 shows the proposed configuration where the bimorph piezoelectric beam is clamped at the middle and is utilized as a receiver for the WPT system. Two permanent magnets are positioned at the two ends of the beam. Their magnetic directions are parallel and in opposite direction to each other. With the use of a circular Helmholtz (CH) coil as a transmitter, a uniform magnetic field generated along the longitudinal axis induces a torque of equal magnitude on each magnet mass, but in opposite directions (i.e. clockwise/anticlockwise and vise versa). As a consequence, two portions of the cantilever beam vibrate like a bird's flapping wings.

The operation of the structure can be represented by an equivalent circuit model as shown in figure 2. The linear two-port equations describing the relation of the transducer force F_T, the charge on the positive electrical terminal q, the displacement at the center of tip mass x and the voltage across the electric terminals V_T are [25, 26]

$$F_T = K_0 x + \Gamma_P V_T, \tag{2.1}$$

$$q = -\Gamma_P x + C_0 V_T, \tag{2.2}$$

where Γ_P is the transduction factor between the mechanical and electrical domains.

The lumped elements of the model are determined as follows [27]

$$M_B = J_r V_M H_{ac}, \tag{2.3}$$

$$F_M = \frac{3}{2}\frac{M_B}{l_{eff}}, \tag{2.4}$$

$$l_{eff} = \frac{L + L_0}{2}, \tag{2.5}$$

$$m = M + \frac{33}{140} m_b, \tag{2.6}$$

$$K_0 = \frac{3(YI)_c}{l_{eff}^3}, \tag{2.7}$$

$$(YI)_c = 2Y_p\left[\frac{wt_p^3}{12} + wt_p\left(\frac{t_s + t_p}{2}\right)^2\right] + Y_s\frac{wt_s^3}{12}, \tag{2.8}$$

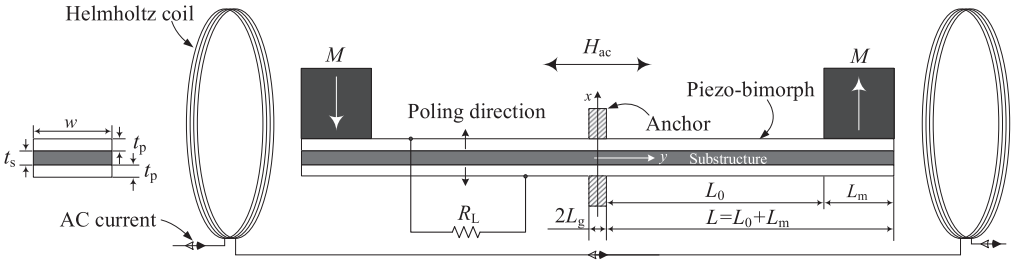

Figure 1. Schematic of the center-clamped bimorph piezoelectric transducer with two magnet tip masses used as a receiver for a low-frequency WPT system.

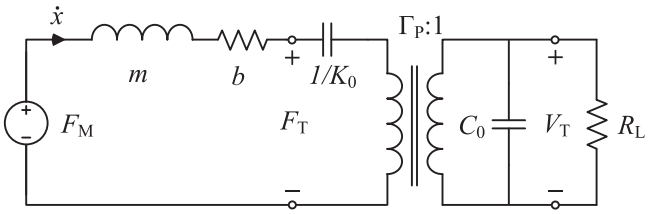

Figure 2. Equivalent two-port model of the piezoelectric transducer.

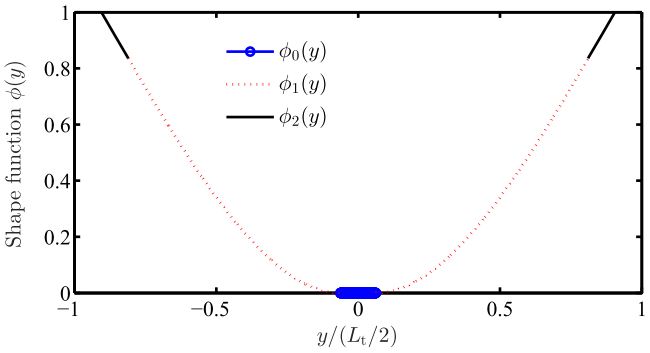

Figure 3. Static deflection shape function $\phi(y)$, here L_t is the total length of the beam, $L_t = 2(L + L_g)$.

$$C_0 = \epsilon_{33}^S \frac{w(L + L_g)}{t_p}, \tag{2.9}$$

where L and L_0 are the intermediate lengths defined as in figure 1, $m_b = wL(2t_p\rho_p + t_s\rho_s)$, $M = \rho_M V_M$, the definitions of other parameters can be found in the Nomenclature section. Differing from our previous work [27], the cantilever beam is clamped at the center instead of one end. In addition, this paper focuses more on the efficiency of a complete transmission system than investigating power optimization issues.

2.2. Static shape function

In the same manner presented by Kim *et al* [28] and Wang *et al* [29], the tip mass is treated as a distributed mass rather than a point mass. While the authors in [28, 29] investigated a piezoelectric EH using the distributed-parameter model, we develop an equivalent linear two-port model instead (it is perhaps the most widely used model for piezoelectric-based devices). An advantage of this method is to express the output power by an explicit form, which is convenient to further interpret the system performance. Assume that the structure is symmetric about the x-axis, the static deflection shape function $\phi(y)$ can be described as follows

$$\begin{aligned}
&0 \leqslant |y| \leqslant L_g\colon \phi_0(y) = 0,\\
&L_g \leqslant |y| \leqslant (L_0 + L_g)\colon \phi_1(y)\\
&= q_m\left(\frac{L_m(L_0 + L)}{4}|y - L_g\mathrm{sign}(y)|^2\right.\\
&\quad\left. - \frac{L_m}{6}|y - L_g\mathrm{sign}(y)|^3\right)\\
&\quad + q_b\left(\frac{L^2}{4}|y - L_g\mathrm{sign}(y)|^2 - \frac{L}{6}|y - L_g\mathrm{sign}(y)|^3\right.\\
&\quad\left. + \frac{1}{24}|y - L_g\mathrm{sign}(y)|^4\right), (L_0 + L_g) \leqslant |y|\\
&\leqslant (L + L_g)\colon \phi_2(y) = q_m\left(\frac{L_0L_mL}{2}|y - L_g\mathrm{sign}(y)|\right.\\
&\quad\left. - \frac{L_0^2L_m(2L + L_m)}{12}\right) + q_b\left(\frac{L_0(L^2 + L_0L_m + 2L_m^2)}{6}\right.\\
&\quad\left. |y - L_g\mathrm{sign}(y)| - \frac{L_0^2(L^2 + 2L_0L_m + 5L_m^2)}{24}\right),
\end{aligned} \tag{2.10}$$

where

$$\begin{aligned}
q_m &= \frac{24}{L_0[2L_m(4L_0^2 + 6L_0L_m + 3L_m^2) + q_r(3L_0^3 + 10L_0^2L_m + 12L_0L_m^2 + 6L_m^3)]},\\
q_b &= q_mq_r, \text{ and } q_r = \frac{L_mm_b}{LM}.
\end{aligned} \tag{2.11}$$

The final static shape function is depicted in figure 3. It should be noted that the vibration displacement of each branch (i.e. $y \leqslant 0$ or $y \geqslant 0$) is exactly the same as using a

single piezoelectric beam correspondingly. However, in a realistic application, if we use two piezoelectric resonators, the electronic interface circuit is required to deal with the challenge of multiple outputs. This may require a more sophisticated complete system. Therefore, utilizing the center-clamped cantilever beam as an alternative is an appropriate option to avoid that issue.

2.3. Modal coupling coefficient

The electromechanical coupling factor is derived based on the static shape function as [30, 31]

$$\begin{aligned}\Gamma_{\mathrm{P}} &= -e_{31}w\frac{t_{\mathrm{p}}+t_{\mathrm{s}}}{2}\int_{-(L+L_{\mathrm{g}})}^{(L+L_{\mathrm{g}})}\frac{\mathrm{d}^2\phi(y)}{\mathrm{d}y^2}\mathrm{d}y \\ &= -e_{31}w\frac{t_{\mathrm{p}}+t_{\mathrm{s}}}{2}\int_{-(L+L_{\mathrm{g}})}^{(L+L_{\mathrm{g}})} \\ &\quad\times\left[\frac{\mathrm{d}^2\phi_0(y)}{\mathrm{d}y^2}+\frac{\mathrm{d}^2\phi_1(y)}{\mathrm{d}y^2}+\frac{\mathrm{d}^2\phi_2(y)}{\mathrm{d}y^2}\right]\mathrm{d}y. \end{aligned} \tag{2.12}$$

Note that $\phi_0(y)=0$ for all y such that $0\leqslant|y|\leqslant L_{\mathrm{g}}$ and $\phi_2(y)$ is a first order polynomial of y for all y such that $(L_0+L_{\mathrm{g}})\leqslant|y|\leqslant(L+L_{\mathrm{g}})$, therefore $\mathrm{d}^2\phi_0(y)/\mathrm{d}y^2=\mathrm{d}^2\phi_2(y)/\mathrm{d}y^2=0$ and (2.12) reduces to

$$\begin{aligned}\Gamma_{\mathrm{P}} &= -e_{31}w\frac{t_{\mathrm{p}}+t_{\mathrm{s}}}{2} \\ &\quad\times\left[\int_{-(L_0+L_{\mathrm{g}})}^{-L_{\mathrm{g}}}\frac{\mathrm{d}^2\phi_1(y)}{\mathrm{d}y^2}\mathrm{d}y+\int_{L_{\mathrm{g}}}^{(L_0+L_{\mathrm{g}})}\frac{\mathrm{d}^2\phi_1(y)}{\mathrm{d}y^2}\mathrm{d}y\right] \\ &= -e_{31}w\frac{t_{\mathrm{p}}+t_{\mathrm{s}}}{2} \\ &\quad\times\left[\frac{\mathrm{d}\phi_1(y)}{\mathrm{d}y}\Bigg|_{y=-(L_0+L_{\mathrm{g}})}^{y=-L_{\mathrm{g}}}+\frac{\mathrm{d}\phi_1(y)}{\mathrm{d}y}\Bigg|_{y=L_{\mathrm{g}}}^{y=(L_0+L_{\mathrm{g}})}\right]. \end{aligned} \tag{2.13}$$

Denote $\kappa=|y-L_{\mathrm{g}}\mathrm{sign}(y)|\geqslant 0$, we can re-write $\phi_1(y)$ as a function of κ as follows

$$\begin{aligned}\phi_1(\kappa) &= q_{\mathrm{m}}\left(\frac{L_{\mathrm{m}}(L_0+L)}{4}\kappa^2-\frac{L_{\mathrm{m}}}{6}\kappa^3\right) \\ &\quad+q_{\mathrm{b}}\left(\frac{L^2}{4}\kappa^2-\frac{L}{6}\kappa^3+\frac{1}{24}\kappa^4\right). \end{aligned} \tag{2.14}$$

This implies that

$$\frac{\mathrm{d}\phi_1(\kappa)}{\mathrm{d}\kappa}\Bigg|_{\kappa=0}=0. \tag{2.15}$$

In addition, $\kappa\overset{y\to\pm L_{\mathrm{g}}}{\longrightarrow}0$, we infer that

$$\frac{\mathrm{d}\phi_1(y)}{\mathrm{d}y}\Bigg|_{y=-L_{\mathrm{g}}}=\frac{\mathrm{d}\phi_1(y)}{\mathrm{d}y}\Bigg|_{y=L_{\mathrm{g}}}=0. \tag{2.16}$$

These results collide with the fact that the cantilever beam is clamped at $y=\pm L_{\mathrm{g}}$ and therefore the derivative of the static displacement $\phi_1(y)$ with respect to y at these positions must equal zero by following the boundary conditions. Formula (2.13) then becomes

$$\Gamma_{\mathrm{P}}=-e_{31}w\frac{t_{\mathrm{p}}+t_{\mathrm{s}}}{2}\frac{\mathrm{d}\phi_1(y)}{\mathrm{d}y}\Bigg|_{y=-(L_0+L_{\mathrm{g}})}^{y=(L_0+L_{\mathrm{g}})}. \tag{2.17}$$

Due to the symmetric property of $\phi_1(y)$, we get

$$\frac{\mathrm{d}\phi_1(y)}{\mathrm{d}y}\Bigg|_{y=-(L_0+L_{\mathrm{g}})}=-\frac{\mathrm{d}\phi_1(y)}{\mathrm{d}y}\Bigg|_{y=(L_0+L_{\mathrm{g}})}. \tag{2.18}$$

The explicit form of the electromechanical coupling is hence expressed as

$$\begin{aligned}\Gamma_{\mathrm{P}} &= -e_{31}w(t_{\mathrm{p}}+t_{\mathrm{s}})\frac{\mathrm{d}\phi_1(y)}{\mathrm{d}y}\Bigg|_{y=(L_0+L_{\mathrm{g}})}=-4e_{31}w(t_{\mathrm{p}}+t_{\mathrm{s}}) \\ &\quad\times\frac{3(M+m_{\mathrm{b}})L^2-3m_{\mathrm{b}}L_0L+m_{\mathrm{b}}L_0^2}{6(M+m_{\mathrm{b}})L^3-6m_{\mathrm{b}}L_0L^2+2L_0^2L(M+2m_{\mathrm{b}})-L_0^3m_{\mathrm{b}}}. \end{aligned} \tag{2.19}$$

Now all the lumped parameters and functions necessary for the model have been obtained.

2.4. Power delivered to a load resistance

Assuming that the piezoelectric resonator is driven by a time harmonic force $F_{\mathrm{M}}(t)=F_0\cos(\omega t)$ of angular frequency ω, the steady-state average power delivered to a load resistance is computed as

$$P_{\mathrm{L}}=\frac{1}{T}\int_0^T\frac{V_{\mathrm{T}}^2(t)}{R_{\mathrm{L}}}\mathrm{d}t=\frac{1}{2}\frac{|V_0|^2}{R_{\mathrm{L}}}, \tag{2.20}$$

where $T=1/f=2\pi/\omega$ is the period of the sinusoidal function $F_{\mathrm{M}}(t)$.

The linear two-port model shown in figure 2 is commonly described by two equations (2.1) and (2.2) [25, 26] where x and V_{T} are independent variables. Other formulations such as the one with x and q as independent variables are [26, 32]

$$F_{\mathrm{T}}=K_1x+\frac{\Gamma_{\mathrm{P}}}{C_0}q, \tag{2.21}$$

$$V_{\mathrm{T}}=\frac{\Gamma_{\mathrm{P}}}{C_0}x+\frac{1}{C_0}q. \tag{2.22}$$

Taking the time derivatives of both sides of equation (2.22) and note that $\dot{q}=-I_{\mathrm{L}}=-V_{\mathrm{T}}/R_{\mathrm{L}}$ (i.e. R_{L} is the load resistance connected directly to the electrical ports and I_{L} is the current through it), we have

$$\dot{V}_{\mathrm{T}}=\frac{\Gamma_{\mathrm{P}}}{C_0}\dot{x}-\frac{V_{\mathrm{T}}}{R_{\mathrm{L}}C_0}. \tag{2.23}$$

Equation (2.23) in the frequency domain is represented by

$$V_0\left(j\omega+\frac{1}{R_{\mathrm{L}}C_0}\right)=j\omega\frac{\Gamma_{\mathrm{P}}}{C_0}X_0, \tag{2.24}$$

where V_0 and X_0 are the complex amplitudes of V_{T} and x respectively. A closed-form of V_0 as a function of X_0 is

$$V_0=\frac{\Gamma_{\mathrm{P}}}{C_0}\frac{j\omega R_{\mathrm{L}}C_0}{1+j\omega R_{\mathrm{L}}C_0}X_0. \tag{2.25}$$

From (2.20), the output power can be written as

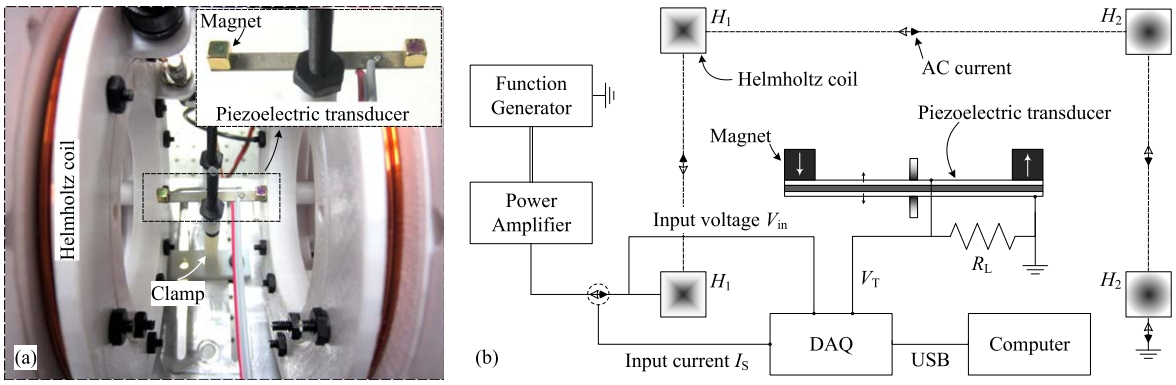

Figure 4. (a) Experimental prototype of the Helmholtz transmitting coil and the piezoelectric/magnet receiver. (b) Sketch of the electrical setup for measuring the input voltage/current V_{in}/I_s and the output voltage V_L across the load resistance R_L. The two coils connected in series are marked by notations H_1 and H_2.

$$P_L = \frac{1}{2}\frac{\Gamma_P^2}{C_0}\frac{\omega^2 R_L C_0}{1+(\omega R_L C_0)^2}|X_0|^2 = \frac{1}{2}\Delta K\frac{\omega^2\tau}{1+(\omega\tau)^2}|X_0|^2, \tag{2.26}$$

where the electrical time scale, the open-circuit stiffness and the difference between the highest and lowest stiffnesses are

$$\tau = R_L C_0, \tag{2.27}$$

$$K_1 = K_0 + \Delta K, \tag{2.28}$$

$$\Delta K = \frac{\Gamma_P^2}{C_0} \tag{2.29}$$

respectively.

Based on equation (2.2), the complex amplitude of the charge Q_0 in the frequency domain is

$$\begin{aligned} Q_0 &= -\Gamma_P X_0 + C_0 V_0 = -\Gamma_P X_0 + \Gamma_P\frac{j\omega\tau}{1+j\omega\tau}X_0 \\ &= -\frac{\Gamma_P}{1+j\omega\tau}X_0. \end{aligned} \tag{2.30}$$

From (2.21), the equation of motion in the mechanical domain is rearranged as

$$m\ddot{x} = -K_1 x - b\dot{x} - \frac{\Gamma_P}{C_0}q + F_0\cos(\omega t). \tag{2.31}$$

Similarly, the equivalent equation in the frequency domain reads as

$$\begin{aligned} -m\omega^2 X_0 &= -K_1 X_0 - j\omega b X_0 - \frac{\Gamma_P}{C_0}Q_0 + F_0 \\ &= -K_1 X_0 - j\omega b X_0 + \Delta K\frac{1}{1+j\omega\tau}X_0 + F_0, \end{aligned} \tag{2.32}$$

which results in

$$X_0 = \frac{F_0}{K_1 - m\omega^2 + j\omega b - \Delta K\frac{1}{1+j\omega\tau}}. \tag{2.33}$$

The squared amplitude of the displacement has the following form

$$|X_0|^2 = \frac{F_0^2}{\left[\omega b + \Delta K\frac{\omega\tau}{1+(\omega\tau)^2}\right]^2 + \left[K_1 - m\omega^2 - \Delta K\frac{1}{1+(\omega\tau)^2}\right]^2}. \tag{2.34}$$

Finally, the explicit form of the output power is

$$\begin{aligned} P_L = &\frac{1}{2}\Delta K\frac{\omega^2\tau}{1+(\omega\tau)^2} \\ &\times \frac{F_0^2}{\left[\omega b + \Delta K\frac{\omega\tau}{1+(\omega\tau)^2}\right]^2 + \left[K_1 - m\omega^2 - \Delta K\frac{1}{1+(\omega\tau)^2}\right]^2}. \end{aligned} \tag{2.35}$$

Formula (2.35) is the main objective to validate the model, where the frequency and **B**-field responses are the most important aspects.

2.5. Measurement and validation

Figure 4(a) shows the Helmholtz coils (transmitter) and the middle-clamped piezoelectric transducer (receiver) used in the experiments, and figure 4(b) illustrates the complete electrical setup. The receiver consists of a bimorph PZT-5A4E cantilever beam with two Neodymium (NdFeB) permanent magnets attached at its tips. The material properties can be found from the datasheets on Piezo System Inc. and K&J Magnetics Inc. websites. The two coils are driven by a Rigol power amplifier while a Tektronix function generator acts as a control unit. The **B**-field generated by the Helmholtz coils is measured by an AC milligauss meter. The current I_s and voltage V_{in} inputted to the coils along with the output voltage V_T induced in the load R_L are collected by a data acquisition (DAQ) unit connected to a computer through USB communication protocol. The average output power is then calculated as $P_L = \frac{1}{T}\int_0^T \frac{V_T^2(t)}{R_L}dt$. The mechanical damping coefficient b is determined by fitting the model simulations to the experimental data at $B_{ac} = 50.77\ \mu$T and $R_L = 1\ \text{M}\Omega$. All the model parameters are now identified and listed in table 1, which are then used for validating all following cases.

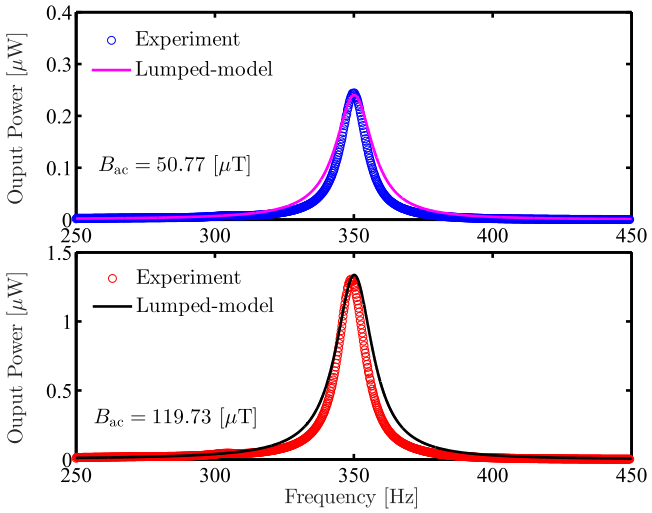

Figure 5. Performance of the WPT system under swept-frequency conditions over a time duration of 60 s.

Table 1. Model parameters, including material properties of (i) Bimorph PZT-5A4E cantilever beam with brass substructure and (ii) neodymium magnets.

Parameters	Value
μ_0	$4\pi \times 10^{-7}$ H m^{-1}
w	3.175 mm
$L_t = 2(L + L_g)$	32.55 mm
$2L_g$	1.90 mm
t_p	0.14 mm
Y_p	66×10^9 Pa
d_{31}	-190×10^{-12} m V^{-1}
C_0	4.83 nF
ρ_p	7800 kg m^{-3}
t_s	0.1 mm
Y_s	100×10^9 Pa
ρ_s	8500 kg m^{-3}
L_m	3.175 mm
ρ_M	8630 kg m^{-3}
J_r	1.45 T
b	18.92×10^{-3} Nsm^{-1}
ζ	1.7%

Figure 5 presents the frequency response of the system with different amplitudes of the applied **B**-field, $B_{ac} = 50.77$ and 119.73 μT. The load is fixed at 1 MΩ. The measured data are compared to the model predictions by formula (2.20), which shows a good agreement between them. In particular, the optimal frequencies f_r observed in experiment and simulation at $B_{ac} = 50.77$ μT are the same at 350 Hz while the other case, $B_{ac} = 119.73$ μT, indicates a slight difference of 1 Hz (i.e. $f_r = 349$ Hz from the experimental results). This can be explained by the fact that the structure is not perfectly symmetric and the anchor is not completely rigid as assumptions of the model. These imperfections could lead to possible slight nonlinearity on the transducer behaviors and energy lost due to plastic deformation. Their effect on system performance is clearer with increasing the external magnetic field (or in other words, the torques acting on the two magnets).

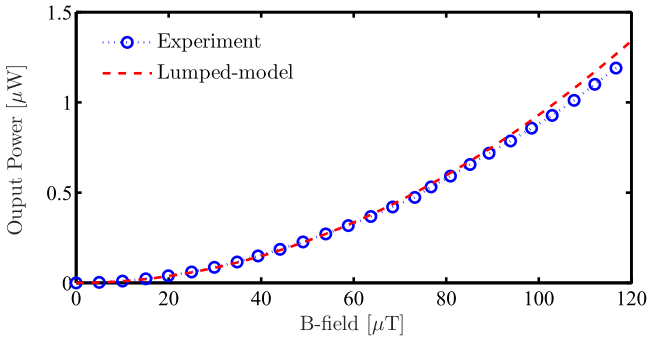

Figure 6. System response with discrete variation of the applied **B**-field while the drive frequency is kept fixed at 350 Hz.

In order to verify the consistency of the model, we choose to drive the WPT system at the fixed frequency $f_r = 350$ Hz and only vary the **B**-field amplitude in a wide range from 0 up to 120 μT. The model-predicted simulations are still in a good agreement with the experimental results as shown in figure 6. It is also confirmed that higher strengths of magnetic field cause larger errors between the predictions and measurements due to slight differences in the actual optimal frequency and the chosen f_r. Although, these differences can be considered almost negligible in practice. In summary, the lumped element model has been successful in explaining behavioral characteristics of the WPT system.

3. Investigation on the efficiency of a WPT system

3.1. Theoretical model

Since the efficient operating frequency range of the center-clamped configuration is typically much less than 1 kHz, the system is considered electromagnetically quasi-static, and therefore the electromagnetic radiation from the coils is neglected. Figure 7 shows a model for investigating the transmission efficiency of a WPT system. Here, V_s and R_s are the source voltage and internal resistance. L_H and R_H represent the total inductance and resistance of the Helmholtz coils. Γ_M is the coupling factor relating the source current I_s and the electromotive force V_{EMF} to the force acting on the piezoelectric-beam F_M and its tip mass velocity $\dot{x}$ respectively. Note that L_H is the sum of each coil inductance L_{C_i} (configured in series) and the mutual inductance M_C between the two coils, i.e. $L_H = L_{C_1} + L_{C_2} + M_C$ [33]. With the fact that the generated **B**-field is proportional to the current through the Helmholtz coil which is dependent on the total inductance L_H, determining specific values of $L_{C_{1/2}}$ and M_C does not affect on the final result, and is not the objective of this paper.

Due to the similarity of the electromechanical/electrodynamic transduction mechanisms: piezoelectric, electrostatic, electromagnetic and ME [26, 34], we aim to develop a unified model that is able to evaluate the system efficiency when one of these resonator types is used as a receiver. Despite the apparent differences, the first three architectures can be described by similar mathematical equations and it is possible to obtain the output power of all the three transducers on the same form, i.e.

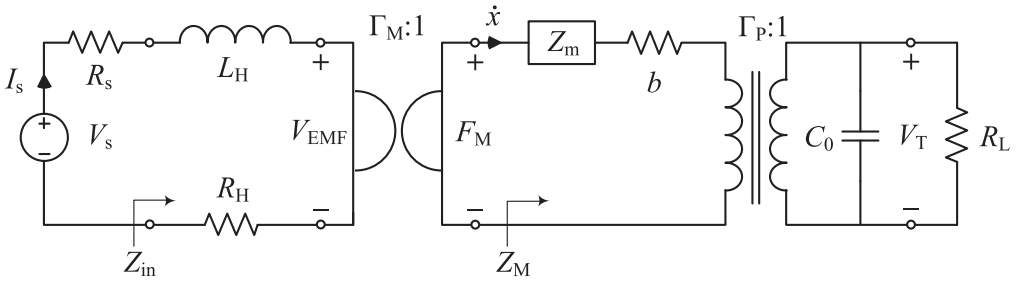

Figure 7. Schematic of lumped element model for wireless power transfer systems with piezoelectric transducer as a receiver.

(2.35). For the electrostatic and piezoelectric generators, the electrical time scale τ and the stiffness difference ΔK are defined by (2.27) and (2.29) respectively. In the case of using the electromagnetic transducer, we perform the following substitutions to get the corresponding output power

$$\tau \to \tau_e = \frac{L_0}{R_L}, \tag{3.1}$$

$$\Delta K \to \Delta K_e = \frac{\Psi^2}{L_0}, \tag{3.2}$$

where L_0 is the clamped inductance and Ψ is the electromagnetic transduction factor. Details of these analyses were thoroughly presented in [26]. We also provide an alternative model along with derivations of the output power and the efficiency in appendix A.

It is worthwhile to note that, for the structure under consideration, the mechanical impedance is explicitly expressed as a mass-spring system

$$Z_m = j(\omega m - K_0/\omega). \tag{3.3}$$

However, in general Z_m is an inseparable function of frequency and material properties. For instance, the impedance of the bimorph piezoelectric/magnetostrictive laminated composite beam vibrating longitudinally under applied magnetic field due to the ME effect is

$$Z_m \to Z_e = j\bar{v}\bar{\rho}A\left(\tan\frac{kL_e}{2} - \frac{1}{\sin(kL_e)}\right). \tag{3.4}$$

An example of the ME device is presented in appendix B.

The generalized forms $Z_m = jZ_0$, τ and ΔK thus will be used for further derivations. The impedance Z_M and Z_{in} in figure 7 are given as follows

$$Z_M = Z_m + b + \Gamma_P^2\frac{R_L}{1 + j\omega R_L C_0} = jZ_0 + b + \Delta K\frac{\tau}{1 + j\omega\tau}, \tag{3.5}$$

$$Z_{in} = j\omega L_H + R_H + \frac{\Gamma_M^2}{Z_M}, \tag{3.6}$$

$$\Re\{Z_{in}\} = R_H + \frac{(\alpha\varphi_m)^2\left[b + \Delta K\frac{\tau}{1+(\omega\tau)^2}\right]}{\left[-Z_0 + \Delta K\frac{\omega\tau^2}{1+(\omega\tau)^2}\right]^2 + \left[b + \Delta K\frac{\tau}{1+(\omega\tau)^2}\right]^2}, \tag{3.7}$$

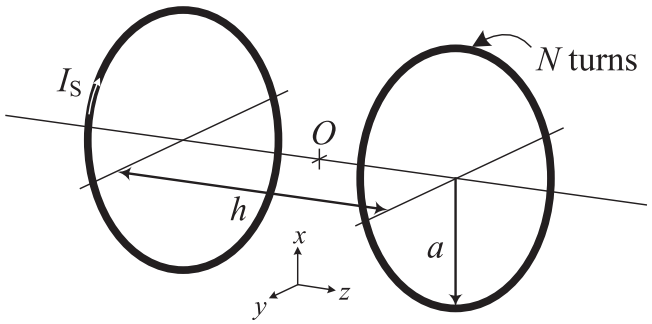

Figure 8. Configuration of circular Helmholtz coil, where the radius of each coil and the distance between them are denoted by a and h respectively which are the same as in [35] for convenience of following derivations.

$$\Im\{Z_{in}\} = \omega L_H - \frac{(\alpha\varphi_m)^2\left[-Z_0 + \Delta K\frac{\omega\tau^2}{1+(\omega\tau)^2}\right]}{\left[-Z_0 + \Delta K\frac{\omega\tau^2}{1+(\omega\tau)^2}\right]^2 + \left[b + \Delta K\frac{\tau}{1+(\omega\tau)^2}\right]^2}. \tag{3.8}$$

The power input to the network and the transmission efficiency are then determined by

$$P_{in} = \frac{1}{2}|V_s|^2\frac{\Re\{Z_{in}\}}{|Z_{in} + Z_s|^2} = \frac{1}{2}|V_s|^2\frac{\Re\{Z_{in}\}}{(R_s + \Re\{Z_{in}\})^2 + (\Im\{Z_{in}\})^2}, \tag{3.9}$$

$$\eta_t = \frac{P_L}{P_{in}}. \tag{3.10}$$

In the considered circumstance, the source impedance is real, $Z_s = R_s$ for the sake of simplification.

We are now considering the CH coil depicted in figure 8, here O is the origin of the rectangular coordinates $Oxyz$. Assume the CH coils are driven by a sinusoidal source, the amplitude of the magnetic flux density **B** right at the middle of the two coils is [35]

$$B_{ac} = B_{ac|x=y=z=0} = \mu_0\alpha|I_s| \tag{3.11}$$

$$\text{where } \alpha = \frac{N}{2}a^2 \times \left[\frac{1}{\left(a^2+\left(z+\frac{h}{2}\right)^2\right)^{3/2}} + \frac{1}{\left(a^2+\left(z-\frac{h}{2}\right)^2\right)^{3/2}}\right] = N\frac{a^2}{\left(a^2+\left(\frac{h}{2}\right)^2\right)^{3/2}}, \tag{3.12}$$

$$\text{and } |I_s| = \left|\frac{V_s}{Z_{in}+R_s}\right| = \frac{|V_s|}{\sqrt{(R_s+\Re\{Z_{in}\})^2+(\Im\{Z_{in}\})^2}}. \tag{3.13}$$

The constant ratio α may be different for various geometries of the coils and the distance between them. However, the relation between the magnetic field strength **H** and the current through the coils can always be written in the form

$$H_{ac} = H_{ac|x=y=z=0} = \alpha|I_s|. \tag{3.14}$$

The matrix representation of the linear two-port gyrator and the electrodynamic coupling coefficient are

$$\begin{bmatrix} F_M \\ V_{EMF} \end{bmatrix} = \begin{bmatrix} \Gamma_M & 0 \\ 0 & \Gamma_M \end{bmatrix}\begin{bmatrix} I_s \\ \dot{x} \end{bmatrix}, \tag{3.15}$$

$$\Gamma_M = \frac{|F_M|}{|I_s|} = \frac{F_0}{|I_s|}. \tag{3.16}$$

Based on the analysis in the previous section, the relationship between the force on the input mechanical port and the **H**-field is derived as follows

$$|F_M| = \varphi_m H_{ac}, \tag{3.17}$$

$$\text{where } \varphi_m = \frac{3}{2}\frac{J_r V_M}{l_{eff}}. \tag{3.18}$$

Substituting (3.14) and (3.17) into (3.16), we get

$$\Gamma_M = \alpha\varphi_m. \tag{3.19}$$

The amplitude of the force F_M now takes the form

$$F_0 = \alpha\varphi_m\frac{|V_s|}{\sqrt{(R_s+\Re\{Z_{in}\})^2+(\Im\{Z_{in}\})^2}}. \tag{3.20}$$

The analytical solution of the power transferred to the load is re-written from (2.20) as

$$P_L = \frac{1}{2}\Delta K\frac{\omega^2\tau}{1+(\omega\tau)^2} \times \frac{F_0^2}{\left[-\omega Z_0 + \Delta K\frac{(\omega\tau)^2}{1+(\omega\tau)^2}\right]^2 + \left[\omega b + \Delta K\frac{\omega\tau}{1+(\omega\tau)^2}\right]^2}, \tag{3.21}$$

where $Z_0 = \omega m - K_0/\omega$. From (3.9), (3.20) and (3.21), the efficiency is provided by

$$\eta_t = \frac{1}{\Re\{Z_{in}\}}\Delta K\frac{\omega^2\tau}{1+(\omega\tau)^2} \times \frac{(\alpha\varphi_m)^2}{\left[-\omega Z_0 + \Delta K\frac{(\omega\tau)^2}{1+(\omega\tau)^2}\right]^2 + \left[\omega b + \Delta K\frac{\omega\tau}{1+(\omega\tau)^2}\right]^2}. \tag{3.22}$$

Since Γ_M is relatively small, the reflected loads from the transmitter onto the piezoelectric cantilever beam and vise versa are neglected, and F_0 is considered as a constant and independent on R_L for the sake of simplification. At the resonance frequency $\omega = \omega_0$, the optimal load and maximum power are

$$^{opt}\tau = \frac{1}{\omega_0\sqrt{M_0^2+1}}, \quad ^{opt}R_L = \frac{1}{\omega_0 C_0\sqrt{M_0^2+1}}, \tag{3.23}$$

$$^{opt}P_L = \frac{1}{4}F_0^2\frac{M_0}{b}(\sqrt{M_0^2+1}-M_0), \tag{3.24}$$

where the resonator figure of merit is defined as a function of frequency

$$M_f = \frac{\Gamma_P^2}{b\omega C_0} \tag{3.25}$$

and at $\omega = \omega_0$, $M_0 = \Gamma_P^2/(b\omega_0 C_0) = \Delta K/(b\omega_0)$. The corresponding efficiency is

$$\eta_t = \frac{1}{2}\frac{(\alpha\varphi_m)^2}{\Re\{Z_{in}\}}\frac{M_0}{b}(\sqrt{M_0^2+1}-M_0) \tag{3.26}$$

$$\text{where } \Re\{Z_{in}\} = R_H + (\alpha\varphi_m)^2\left(2-\frac{M_0}{\sqrt{M_0^2+1}}\right). \tag{3.27}$$

$\Re\{Z_{in}\}$ is obtained by substituting $\omega = \omega_0$, $\Delta K = b\omega_0 M_0$ and (3.23) into (3.7).

The analytical model (i.e. formulas (3.21) and (3.22)) can be used as a general framework for estimating the output power and the transfer efficiency of any electromechanical/electrodynamic-based WPT system. A summary of the corresponding definitions of Z_0, τ (τ_e) and ΔK (ΔK_e) for different types of generators is listed in table 2.

3.2. Experimental validation

The aim of this section is to describe the characterization of the Helmholtz coils along with identification of the electrodynamic coupling factor and to validate the complete lumped-element model for predicting the efficiency.

The electrical properties of the transmitter, such as the coil inductance L_H and resistance R_H, as well as the source impedance R_s, are measured separately without mounting them on the experimental setup to avoid any possible dynamic interferences with the magnets. Meanwhile, the coefficient α is extracted after construction of the complete system. To be more specific, α is achieved by a linear fit between measured data of the input current I_s and the generated **B**-field as shown in figure 9. The average-experimental-input power is calculated as $P_{in} = \frac{1}{2}|V_{in}||I_s|\cos\phi$ where the method to measure V_{in} and I_s is presented in figure 4 and ϕ [rad s^{-1}] is the phase difference between them. The experimental efficiency is then simply obtained by (3.10). The additional system parameters are listed in table 3.

Figure 10 presents the variation of the input current and power in terms of frequency with different values of the voltage source amplitude $|V_s| = 100$ mV and 240 mV. Since the main purpose is to verify the proposed model, $|V_s|$ is chosen arbitrarily and the **B**-field amplitude is measured

Table 2. Corresponding definitions of the mechanical impedance, the electrical time scale and the stiffness difference of four transducer types used in formulas (3.21) and (3.22).

Parameters	Magnetoelectric	Piezoelectric/Electrostatic	Electromagnetic
Z_0	$\bar{v}\bar{\rho}A(\tan(kL_e/2) - 1/\sin(kL_e))$	$\omega\, m - K_0/\omega$	$\omega\, m - K_0/\omega$
τ (τ_e)	$R_L\, C_0$	$R_L\, C_0$	L_0/R_L
ΔK (ΔK_e)	Γ_P^2/C_0	Γ_P^2/C_0	Ψ^2/L_0

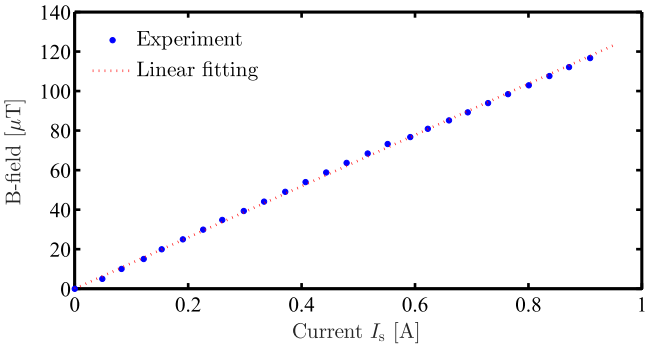

Figure 9. Linear fit of the relationship between the input current I_s and the generated **B**-field.

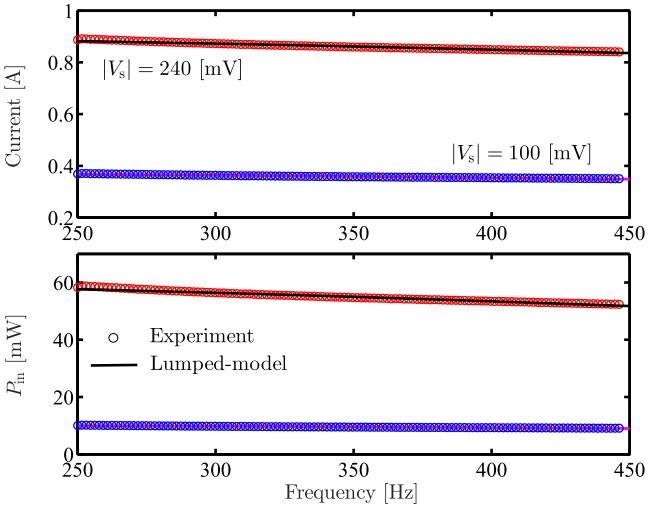

Figure 10. Comparison between the measured current amplitude $|I_s|$ and average power P_{in} input to the network and the predictions from model.

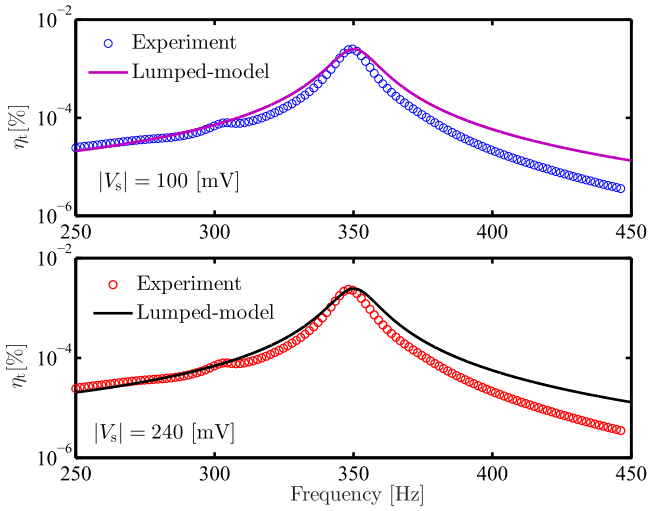

Figure 11. Frequency responses of the transmission efficiency with different source voltages.

Table 3. Model parameters (cont'd).

Parameters	Value
R_H	148.16 mΩ
L_H	39.10 μH
R_s	116.82 mΩ
α	129.60 μT A^{-1}

accordingly. We use the internal resistance of the DAQ unit (1 MΩ) as the load resistance in order to avoid the error as much as possible. The corresponding input voltage amplitudes of the two cases are $|V_{in}| \approx 150$ and 30 mV, and the cosine of the phase difference between the input voltage and the input current is $\cos\phi \approx 0.89$, approximately. The experimental results are compared to those of the model computed using (3.9) and (3.13), showing a good agreement between the theoretical results and measurements. The analytical model (i.e. formula (3.22)) also accurately predicts the measured efficiency as can be seen in figure 11. It should be noted that η_t is independent of the strength of the applied **B**-field, or in other words, the current input to the two coils. Therefore, the transfer efficiency is a constant with respect to AC magnetic flux density.

3.3. Essential influence of the transmitter coil resistance

For a given system where the parameters and properties of the transmitter coil and the piezoelectric-resonator receiver are determined, (3.24) and (3.26) describe the maximum power delivered to the load (**B**-field dependent) and the corresponding optimum efficiency (**B**-field independent). For convenience, we denote the real part of the input impedance in (3.27) as $\Re\{Z_{in}\} = R_H + \nu\Gamma_M^2 = R_H + \nu(\alpha\varphi_m)^2$ where $\nu = 2 - M_0/\sqrt{M_0^2 + 1}$. In a weak coupling regime $\Gamma_M \to 0$, the second term of $\Re\{Z_{in}\}$ is nearly negligible comparing to the coil resistance $R_H \gg \nu\Gamma_M^2$, thus $\Re\{Z_{in}\} \approx R_H$. This observation indicates that

$$\eta_t \approx \frac{1}{2}\frac{(\alpha\varphi_m)^2}{R_H}\frac{M_0}{b}(\sqrt{M_0^2 + 1} - M_0) \tag{3.28}$$

and therefore $\eta_t \propto \frac{1}{R_H}$.

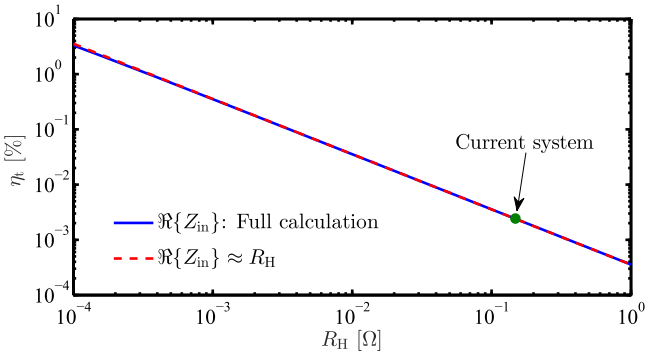

Figure 12. Efficiency as a function of the parasitic resistance R_H of the coil. The maximum output power is given by (3.24) with the optimal load (3.23). The optimum efficiency is computed by (3.26) for two cases: (i) full calculation of $\Re\{Z_{in}\}$ using (3.27), and (ii) an approximation $\Re\{Z_{in}\} \approx R_H$.

In particular, figure 12 shows the theoretical computation of the efficiency as a function of total parasitic resistance of the two coils R_H using (3.26) and (3.28). The obtained results are almost identical for the two cases, hence (3.28) can be utilized as an alternative to estimate the efficiency of a loosely coupled system. The effect of R_H on η_t is significant while that of R_s is almost zero. This is to be expected since we define η_t as a ratio between the power delivered to the load P_L and the power input to the network P_{in} rather than the power available from the source $P_{avs} = \frac{1}{8}\frac{|V_s|^2}{\Re\{Z_s\}} = \frac{1}{8}\frac{|V_s|^2}{R_s}$. It is observed that, for instance, η_t increases by more than two orders of magnitude in comparison to the presented experimental system if R_H decreases to 1 mΩ. Using a higher conductivity material for the coils is not practical. Instead, a doubling of the wire diameter could increase the efficiency by a factor of 4 approximately (i.e. the change of the coil geometry is neglected).

In comparison with other types of WPT systems (e.g. magnetic resonance/induction coupling, capacitive coupling), the efficiency of the proposed structure is low. Despite this obvious drawback, an advantage of the MME system under investigation is that the applied magnetic field can be higher at the low frequencies required by the MME system while still remaining within safe limits [36]. According to the IEEE standards, a maximum allowable field at 1 kHz is ⩾2 mT [13], 10 times larger than the ∼200 μT permissible at 1 MHz [14]. Especially in the case that the receiver is blocked by a metal plate, high frequency devices such as inductive/capacitive coupled systems cannot be utilized due to the effects of eddy currents (i.e. also called Foucault currents, which flow in closed loops within conductors, and in planes perpendicular to the applied magnetic field) [37]. Meanwhile, the MME receiver is able to operate effectively since its resonance frequency is typically lower than 1 kHz and can be reduced to the range of a few hundred Hz by adjusting the structure geometry.

3.4. Method to increase the electrodynamic transduction factor: an example

From (3.19), (3.26) and (3.27), we see that, when $\Gamma_M \to +\infty$ (or large enough), the second term in (3.27) is dominant,

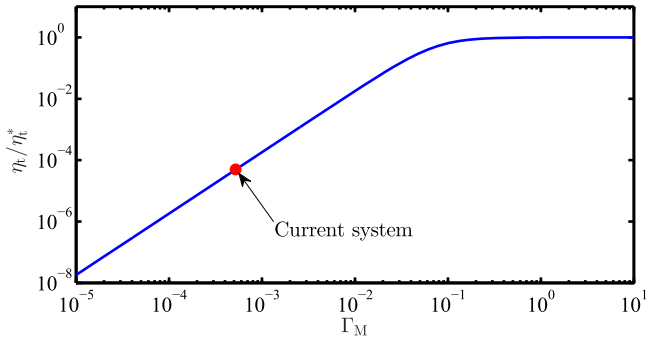

Figure 13. Variations of the efficiency as a function of the electrodynamic transduction factor.

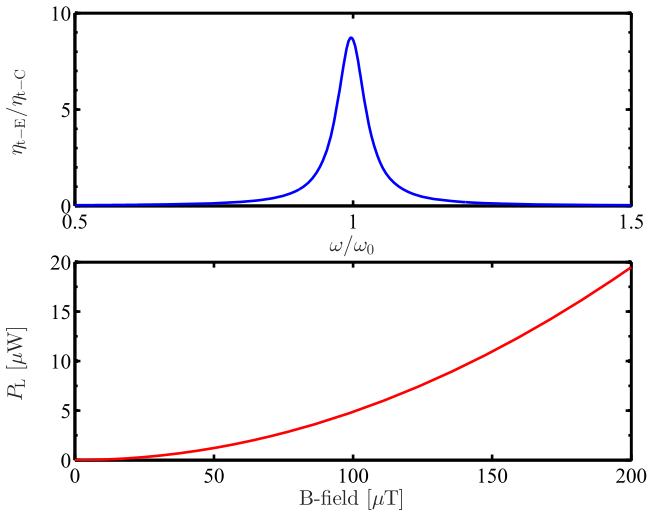

Figure 14. Simulation results of the example structure, denoting the simulated efficiency and the maximum efficiency of the system used in measurements as η_{t-E} and η_{t-C} respectively.

$\nu\Gamma_M^2 \gg R_H$, therefore $\Re\{Z_{in}\} \approx \nu\Gamma_M^2$ and

$$\eta_t \to \eta_t^* = \frac{1}{2}\frac{M_0}{\nu b}(\sqrt{M_0^2+1} - M_0) = \frac{M_0}{2}\frac{(\sqrt{M_0^2+1} - M_0)^2 + 1}{2\sqrt{M_0^2+1} - M_0}. \quad (3.29)$$

Considering Γ_M as a variable and treating the other parameters such as ω_0, C_0, b and Γ_P as constants, the variation of η_t over a wide range of Γ_M is depicted in figure 13.

Obviously, there is still significant room for improvement of the transmission efficiency by increasing Γ_M. An example is presented as follows.

Based on the dependency of the electrodynamic coupling factor Γ_M on the geometry of the Helmholtz coil (a, h), volume of the magnet tip mass V_M and effective length l_{eff} of the piezoelectric cantilever beam (i.e. as presented in (3.12), (3.18) and (3.19)), we found that the efficiency η_t can be increased by a factor of ∼8.7 if we simultaneously double magnet volume ${}^sV_M = 2V_M$, halve the beam length ${}^sL_t = L_t/2$ and optimize the coil radius ${}^sa = h\sqrt{2}/2$, where ${}^sa$ is the stationary point of α and is determined by $\partial\alpha/\partial a = 0$. Here, values with a superscript (i.e. ${}^sX$) are used for

simulations. The Helmholtz coil used in experiments has the ratio of $a \approx 2h$, and the optimal coil provides ${}^{s}\alpha = 1.65\alpha$. The final simulated results of the example are shown in figure 14. The frequency response of the efficiency is normalized by the ratio between the obtained efficiency η_{t-E} and the maximum efficiency of the current system η_{t-C}. The optimal load is given in (3.23). The maximum output power of the optimized system is about 19.5 μW at the magnetic field amplitude of 200 μT, which is sufficient to power various body wireless sensors [38]. This model-based study suggests a potential of significant improvement in the delivered power and is the preliminary work for realizing an optimal system.

In order to prove the feasibility of the optimization method in practice, we investigate the output power when utilizing the same piezoelectric resonator and doubling the magnet volume, in which two magnet masses are placed on top and bottom (symmetric about the y-axis) in each portion of the beam. The measured power in this case is $P_L = 4.93\ \mu$W attained at a resonance frequency of $f_0 = 259.8$ Hz, which is very close to that predicted by the model, $P_L = 4.95\ \mu$W at $f_0 = 256.0$ Hz. The applied $\mathbf{B}-$field amplitude is $B_{ac} = 129\ \mu$T and the load resistance is $R_L = 1\ \text{M}\Omega$. The obtained power is 3.2 times as large as that of the original prototype.

It should be noted that, η_t^* is not the upper bound of the efficiency. η_t^* is the limit of η_t only for the case in which (i) the transducer characteristics (ω_0, C_0), the mechanical damping coefficient b and the electromechanical transduction factor Γ_P were defined, and (ii) the optimal load in (3.23) is used. Furthermore, (3.26) is expressed in terms of architecture-independent parameters such as the resonance frequency ω_0 or the resonator figure of merit M_0 (i.e. at $\omega = \omega_0$). In general, when maximizing the transmission efficiency that is subject to particular limitations or requirements of a realistic application, all geometry-dependent relations (e.g., the dependency of the coil resistance on its length, radius and material properties) need to be taken into consideration. This design problem is out of scope of the paper and is open for future work. However, the analyses reported in section 3.1 can still be used as a framework to solve for the global optimal solution of η_t. For instance, one can describe α, ω_0 and M_0 in (3.26) as functions of geometry, then optimize the corresponding efficiency in terms of those geometric parameters, subject to their constraints (if any).

4. Conclusions

In this work, we presented a WPT device concept using a center-clamped piezo-bimorph transducer with two magnet tip masses as a receiver and a Helmholtz coil as a transmitter. Two equivalent circuit models for exploring the power delivered to the load and the transmission efficiency were developed and experimentally validated. Comparisons between the theoretical simulations and experimental data for different cases (i.e. frequency/$\mathbf{B}$-field responses) showed the accuracy and consistency of both models. Note that the proposed structure requires deliberately aligning so that the piezoelectric beam is clamped at the center. Otherwise, the length difference between the two halves may lead to their mis-matched resonance frequencies. As a consequence, they may have a small phase difference at the operational frequency, which reduces the output power. While the paper analyzed the piezoelectric generator, other electromechanical mechanisms (electrostatic and electromagnetic) or a ME device can be utilized as well and the two models still hold for those energy conversion techniques due to their similarities. Several methods were mentioned to improve the system efficiency such as increasing the wire diameter or the electrodynamic coupling factor. Enhancing electromechanical coupling factor by the use of appropriate piezoelectric materials could be also a potential solution, however, this issue is beyond the scope of the paper and is open for further study.

Acknowledgments

The authors want to thank the anonymous reviewers for their comments on the manuscript.

This work was supported by the National Science Foundation ASSIST Nanosystems ERC under Award Number EEC-1160483.

Appendix A. A model for electromagnetic (electrodynamic) transducer

The physical analogy between the electromagnetic, electrostatic and piezoelectric generators was thoroughly explained in [26] where the three types of resonators were modeled as a lossless transformer. Differing from that, we presents an alternative model of the electromagnetic transducer using an ideal gyrator [25], and then utilize a circuit-theory-based technique to obtain the same closed-form of the output power and efficiency as in (3.21) and (3.22).

The complete model is shown in figure A1, in which the complex amplitudes of the tip mass velocity, the force on the mechanical port and the voltage induced on the electrical port are denoted by V_m, F_Ψ and V_Ψ respectively. The impedance Z_M is calculated as

$$\begin{aligned} Z_M &= j\left(\omega m - \frac{K_0}{\omega}\right) + b + \frac{\Psi^2}{j\omega L_0 + R_L} \\ &= jZ_0 + b + \Delta K_e \frac{\tau_e}{1 + j\omega\tau_e}, \end{aligned} \tag{A.1}$$

where τ_e and ΔK_e are defined in (3.1) and (3.2). We see that the compact form of (A.1) is identical to (3.5), and therefore the expression of the input impedance Z_{in} is unchanged. With a time harmonic drive force $F_M(t) = F_0\cos(\omega t)$ of angular frequency ω, the transverse velocity of the tip mass is

$$V_m = \frac{F_0}{Z_M}. \tag{A.2}$$

The relation between the mechanical velocity and the induced voltage is

$$V_\Psi = \Psi V_m. \tag{A.3}$$

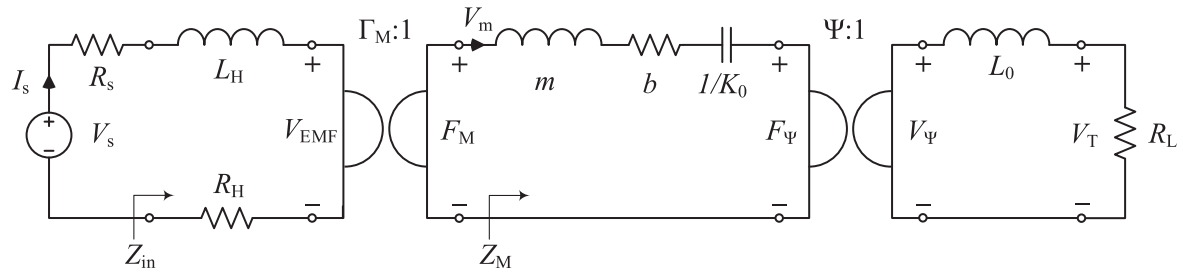

Figure A1. Schematic of lumped element model for wireless power transfer systems with electromagnetic (electrodynamic) transducer as a receiver.

The transducer voltage across the load resistance is

$$V_T = \frac{V_\Psi R_L}{j\omega L_0 + R_L}. \tag{A.4}$$

The power transferred to the load is then given by

$$P_L = \frac{1}{2}\frac{|V_T|^2}{R_L} = \frac{1}{2}\frac{|V_\Psi|^2}{L_0}\frac{L_0/R_L}{1+(\omega L_0/R_L)^2} = \frac{1}{2}\Delta K_e \frac{\omega^2\tau_e}{1+(\omega\tau_e)^2}\frac{F_0^2}{(\omega|Z_M|)^2} \tag{A.5}$$

$$= \frac{1}{2}\Delta K_e \frac{\omega^2\tau_e}{1+(\omega\tau_e)^2} \times \frac{F_0^2}{\left[-\omega Z_0 + \Delta K_e \frac{(\omega\tau_e)^2}{1+(\omega\tau_e)^2}\right]^2 + \left[\omega b + \Delta K_e \frac{\omega\tau_e}{1+(\omega\tau_e)^2}\right]^2}, \tag{A.6}$$

whose form is exactly the same as (3.21).

Either the two-port equations shown in section 2.4 or the circuit theory-based approach presented here can be applied to investigate the output power and the transmission efficiency of any transducer presented in this paper. Both methods yield identical results due to the fact that they are just different techniques of describing the same physical mechanism. While the former clearly describes the insight through the Newton's second law and the Ohm's law, the latter is more convenient and easier for derivations and is more familiar to electrical engineers. Finally, a single expression of each P_L and η_t obtained in section 3.1 can cover all four different types of generators.

Appendix B. ME WPT system

Figure B1 illustrates a configuration of the ME generator, in which two piezoelectric layers are parallel poled in transverse direction (y-axis) and a magnetostrictive shim is magnetized in longitudinal direction (z-axis). When a time-harmonic external magnetic field is applied longitudinally, a longitudinal vibration is excited in the shim due to magnetostrictive effect. It is then elastically coupled to the two piezoelectric layers, causing a forced oscillation in them and inducing a voltage across the load resistance R_L. Similar to the work published by Dong *et al* [34, 39, 40], the complete ME-based WPT system can be modeled by an equivalent circuit shown in figure 7 (note that $\dot{x}$ now denotes the mechanical velocity in the longitudinal direction instead of the transverse vibration). However, differing from those works, the ME cantilever beam is clamped at one end rather than utilizing the free-free configuration (which is widely used in sensing systems). Furthermore, while those authors concerned with the ME voltage coefficient (i.e. the relation between the open circuit voltage and the applied magnetic field or magnetic flux density), we focus more on the power delivered to the load which makes the derivations more complicated.

Following the same procedure reported in [34], the model parameters are derived as follows

$$n = \frac{2t_p}{2t_p + t_m},\ 0 < n < 1, \tag{B.1}$$

$$\bar{\rho} = \rho_p n + \rho_m(1-n), \tag{B.2}$$

$$\bar{v}^2 = \left(\frac{n}{s_{11}^E} + \frac{1-n}{s_{33}^H}\right)\Big/\bar{\rho}, \tag{B.3}$$

$$k^2 = \frac{\omega^2}{\bar{v}^2}, \tag{B.4}$$

$$\Gamma_P = w\frac{d_{31,p}}{s_{11}^E}, \tag{B.5}$$

$$\varphi_m = wt_m\frac{d_{33,m}}{s_{33}^H}, \tag{B.6}$$

$$C_0 = \frac{1}{2}\epsilon_{33}^S\frac{wL_e}{t_p}, \tag{B.7}$$

$$A = (2t_p + t_m)w, \tag{B.8}$$

$$Z_e = j\bar{v}\bar{\rho}A\left(\tan\left(\frac{kL}{2}\right) - \frac{1}{\sin(kL)}\right), \tag{B.9}$$

where ρ_p and ρ_m are the mass densities of the piezoelectric and the magnetostrictive layers respectively, the definitions of w, t_p and t_m are shown in figure B1, ω is the angular driving frequency, s_{11}^E is the elastic compliance of the piezoelectric material under constant electric field, $d_{31,p}$ is the transverse electric constant, s_{33}^H is the elastic compliance at constant magnetic field, $d_{33,m}$ is the longitudinal piezoelectric constant, ϵ_{33}^S is the permittivity component at constant strain with the plane-stress assumption of a thin beam. Γ_M is calculated as in (3.19). The resonance frequency is attained by setting $Z_e = 0$, resulting in

$$\omega_0 = \frac{\pi}{2}\frac{\bar{v}}{L_e}. \tag{B.10}$$

After determining all the key parameters, the explicit solutions of the output power and the transmission efficiency can be obtained

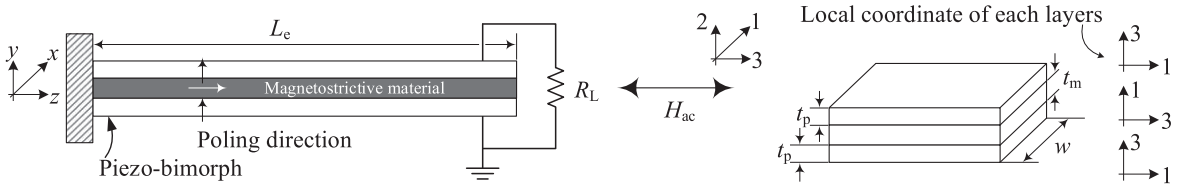

Figure B1. Schematic of magneto-electric transducer and geometric dimensions of the composite laminate.

by substituting them into (3.21) and (3.22). This example completes the analysis in section 3.1.

ORCID iDs

Binh Duc Truong https://orcid.org/0000-0001-7108-4713

References

[1] Roundy S and Wright P K 2004 A piezoelectric vibration based generator for wireless electronics *Smart Mater. Struct.* **13** 1131–42

[2] Mitcheson P 2010 Energy harvesting for human wearable and implantable bio-sensors *Annual International Conference of the IEEE Engineering in Medicine and Biology (31 Aug–4 Sept 2010 3432–36*

[3] Erturk A and Inman D 2011 *Piezoelectric Energy Harvesting* (New York: Wiley) (https://doi.org/10.1002/9781119991151)

[4] Kurs A, Karalis A, Moffatt R, Joannopoulos J D, Fisher P and Soljačić M 2007 Wireless power transfer via strongly coupled magnetic resonances *Science* **317** 83–6

[5] Sid A, Xiaofang Y and Shanhui F 2017 Robust wireless power transfer using a nonlinear parity-time-symmetric circuit *Nature* **546** 6

[6] Paul K and Sarma A K 2018 Fast and efficient wireless power transfer via transitionless quantum driving *Sci. Rep.* **8** 12

[7] Riemer R and Shapiro A 2011 Biomechanical energy harvesting from human motion: theory, state of the art, design guidelines, and future directions *J. NeuroEng. Rehabil.* **8** 22

[8] Ylli K, Hoffmann D, Willmann A, Becker P, Folkmer B and Manoli Y 2015 Energy harvesting from human motion: exploiting swing and shock excitations *Smart Mater. Struct.* **24** 025029

[9] Challa V R, Mur-Miranda J O and Arnold D P 2012 Wireless power transmission to an electromechanical receiver using low-frequency magnetic fields *Smart Mater. Struct.* **21** 115017

[10] Song M, Belov P and Kapitanova P 2017 Wireless power transfer inspired by the modern trends in electromagnetics *Appl. Phys. Rev.* **4** 021102

[11] Huang L, Hu A P, Swain A, Kim S and Ren Y 2013 An overview of capacitively coupled power transfer—a new contactless power transfer solution *2013 IEEE 8th Conf. on Industrial Electronics and Applications (ICIEA)* pp 461–5

[12] Barman S D, Reza A W, Kumar N, Karim M E and Munir A B 2015 Wireless powering by magnetic resonant coupling: recent trends in wireless power transfer system and its applications *Renew. Sustain. Energy Rev.* **51** 1525–52

[13] IEEE 2002 Ieee standard for safety levels with respect to human exposure to electromagnetic fields, 0–3 kHz *IEEE Std C95.6-2002* pp 1–0

[14] IEEE 2006 IEEE standard for safety levels with respect to human exposure to radio frequency electromagnetic fields, 3 kHz to 300 gHz *IEEE Std C95.1-2005 (Revision of IEEE Std C95.1-1991)* pp 1–238

[15] McEachern K M and Arnold D P 2013 Electrodynamic wireless power transmission to a torsional receiver *J. Phys.: Conf. Ser.* **476** 012004

[16] Garraud A, Jimenez J D, Garraud N and Arnold D P 2014 Electrodynamic wireless power transmission to rotating magnet receivers *J. Phys.: Conf. Ser.* **557** 012136

[17] Garraud N, Alabi D, Chyczewski S, Varela J D, Arnold D P and Garraud A 2018 Extending the range of wireless power transmission for bio-implants and wearables *J. Phys.: Conf. Ser.* **1052** 012023

[18] Paprotny I, Xu Q, Chan W W, White R M and Wright P K 2013 Electromechanical energy scavenging from current-carrying conductors *IEEE Sens. J.* **13** 190–201

[19] Guoxi L, Penghong C and Shuxiang D 2014 Energy harvesting from ambient low-frequency magnetic field using magneto-mechano-electric composite cantilever *Appl. Phys. Lett.* **104** 032908

[20] Han J, Hu J, Wang S X and He J 2014 Magnetic energy harvesting properties of piezofiber bimorph/ndfeb composites *Appl. Phys. Lett.* **104** 093901

[21] Lasheras A, Gutiérrez J, Reis S, Sousa D, Silva M, Martins P, Lanceros-Mendez S, Barandiarán J M, Shishkin D A and Potapov A P 2015 Energy harvesting device based on a metallic glass/pvdf magnetoelectric laminated composite *Smart Mater. Struct.* **24** 065024

[22] Ming L C, Xin Z, Junran X, Srinivasan G, Jiefang L and Viehland D 2016 Power conversion efficiency and resistance tunability in coil-magnetoelectric gyrators *Appl. Phys. Lett.* **109** 202907

[23] Reis S, Silva M P, Castro N, Correia V, Rocha J G, Martins P, Lasheras A, Gutierrez J and Lanceros-Mendez S 2016 Electronic optimization for an energy harvesting system based on magnetoelectric metglas/poly(vinylidene fluoride)/metglas composites *Smart Mater. Struct.* **25** 085028

[24] Malleron K, Gensbittel A, Talleb H and Ren Z 2018 Experimental study of magnetoelectric transducers for power supply of small biomedical devices *Microelectronics Journal* 1–6 Article in press

[25] Tilmans H A C 1996 Equivalent circuit representation of electromechanical transducers: I. Lumped-parameter systems *J. Micromech. Microeng.* **6** 157–76

[26] Halvorsen E 2016 Optimal load and stiffness for displacement-constrained vibration energy harvesters arXiv:1603.01909

[27] Truong B D, Williams S and Roundy S 2018 Experimentally validated model and power optimization for piezoelectric-based wireless power transfer systems (in preparation)

[28] Kim J E and Kim Y Y 2011 Analysis of piezoelectric energy harvesters of a moderate aspect ratio with a distributed tip mass *J. Vibr. Acoust. Stress Reliab. Des.* **133**

[29] Wang Y, He H and Xu R 2015 An analytical model for a piezoelectric vibration energy harvester with resonance frequency tunability *Adv. Mech. Eng.* **7**

[30] Erturk A and Inman D J 2009 An experimentally validated bimorph cantilever model for piezoelectric energy harvesting from base excitations *Smart Mater. Struct.* **18** 025009

[31] Kim M, Hoegen M, Dugundji J and Wardle B L 2010 Modeling and experimental verification of proof mass effects on vibration energy harvester performance *Smart Mater. Struct.* **19** 045023

[32] Le C P and Halvorsen E 2012 Mems electrostatic energy harvesters with end-stop effects *J. Micromech. Microeng.* **22** 074013

[33] Javor E R and Anderson T 1998 Design of a helmholtz coil for low frequency magnetic field susceptibility testing *1998 IEEE EMC Symp. Int. Symp. on Electromagnetic Compatibility. Symp. Record (Cat. No.98CH36253)* vol 2 pp 912–7

[34] Dong S, Li J-F and Viehland D 2003 Longitudinal and transverse magnetoelectric voltage coefficients of magnetostrictive/piezoelectric laminate composite: theory *IEEE Trans. Ultrason., Ferroelectr. Freq. Control* **50** 1253–61

[35] Restrepo A F, Franco E, Cadavid H and Pinedo C R 2017 A comparative study of the magnetic field homogeneity for circular, square and equilateral triangular helmholtz coils *2017 Int. Conf. Electrical, Electronics, Communication, Computer, and Optimization Techniques (ICEECCOT)* pp 13–20

[36] Garraud A and Arnold D P 2016 Advancements in electrodynamic wireless power transmission *2016 IEEE Sensors* pp 1–3

[37] Ding-Xin Y, Zheng H, Hong Z, Hai-Feng H, Yun-Zhe S and Bao-Jian H 2015 Through-metal-wall power delivery and data transmission for enclosed sensors: a review *Sensors* **15** 12

[38] Rajan R 2012 Ultra-low power short range radio transceivers White Paper—Microsemi https://www.microsemi.com/document-portal/doc_view/127466-white-paper-ultra-low-power-short-range-radio-transceivers

[39] Dong S, Li J-F and Viehland D 2003 Giant magneto-electric effect in laminate composites *IEEE Trans. Ultrason., Ferroelectr. Freq. Control* **50** 1236–9

[40] Liu G, Zhang C, Chen W and Dong S 2013 Eddy-current effect on resonant magnetoelectric coupling in magnetostrictive-piezoelectric laminated composites *J. Appl. Phys.* **114** 027010